WILEY-VCH

DOI: 10.1002/((please add manuscript number))
Article type: Communication

Selective CO_2 Reduction on Two-Dimensional Mesoporous Bi Nanosheets

Hui Yang[†], Na Han[†], Jun Deng, Jinghua Wu, Yu Wang, Yongpan Hu, Pan Ding, Yafei Li, Yanguang Li and Jun Lu**

Miss. H. Yang, Dr. N. Han, Mr. J. Deng, Dr. J. H. Wu, Mr. Y. P. Hu, Mr. P. Ding, and Prof. Y. G. Li
Institute of Functional Nano & Soft Materials (FUNSOM)
Jiangsu Key Laboratory for Carbon-Based Functional Materials and Devices
Soochow University, Suzhou 215123, China
E-mail: yanguang@suda.edu.cn

Dr. Y. Wang, Prof. Y. F. Li
College of Chemistry and Materials Science
Nanjing Normal University
Nanjing 210023, China

Dr. J. Lu
Chemical Sciences and Engineering Division
Argonne National Laboratory
9700 Cass Ave, Lemont, IL 60439, USA
E-mail: junlu@anl.gov

[†] These two authors contribute equally.

Abstract: The conversion of CO_2 to value-added products using electrical or solar energy represents an attractive means for the capture and utilization of atmospheric CO_2. Formate is a popular product from CO_2 reduction, but its reaction selectivity is usually unsatisfactory. Tin-based materials have attracted most attention for formate production at present. Unfortunately, most of them only exhibit moderate selectivity in a narrow and highly cathodic potential window. In this study, we demonstrate that traditionally under-explored bismuth has a much greater potential for formate production than tin or other materials. Mesoporous bismuth nanosheets are prepared here by the cathodic transformation of atomic-thick bismuth oxycarbonate nanosheets. They enable the selective CO_2 reduction to formate with large current density, excellent Faradaic efficiency (~100%) over a broad potential window and great operation stability. Moreover, we integrate Bi nanosheets with an oxygen evolution

reaction electrocatalyst in full cells, and achieve efficient and robust solar conversion of CO_2/H_2O to formate/O_2.

Keywords: CO_2 reduction, formate, bismuth, mesoporous nanosheets, selectivity

Natural photosynthesis converts solar energy, CO_2 and H_2O into carbohydrates and releases oxygen, which — even though not impressively efficient (with an efficiency of <1% in most plants) — is the very basis of all life forms and human activities, directly or indirectly.[1, 2] Inspired by Mother Nature, researchers around the world have been actively pursuing artificial photosynthesis in the past several decades.[3-5] It is advocated that this process, if realized to its full potential, can make a significant contribution to our future energy supply. One of the key components in the design of efficient artificial photosynthetic systems is the electrocatalysts for CO_2 reduction reaction (CO_2RR).[6-13] They enable the electrochemical transformation of CO_2 to value-added chemical fuels, storing electrical or solar energy in chemical bonds. Formate is a common CO_2RR product. Compared to gaseous products such as CO and hydrocarbons, it has the advantage of easy storage and transportation.[14] Formate is also an important chemical intermediate and renewable energy carrier.[15, 16] Among several candidates reported so far for formate production, Sn-based materials attract the most attention, and yet their activity and selectivity are far from satisfactory.[10, 11] For example, most Sn-based electrocatalysts exhibit moderate formate selectivity (with a peak value between 50-80%) only in a very narrow and highly cathodic potential ($\eta \sim 1$ V) region.[17-20]

Bi locates close to those traditional formate-producing metals (Pb, Cd, Hg, In, Sn and Tl, as first described by Hori[21]) in periodic table, and is therefore expected to have a great potential for CO_2RR. It also distinguishes itself from other heavy metals by virtue of its environmental benignity and unusually low toxicity. The CO_2RR performance of Bi was first brought to people's attention through the pioneering research by Komatsu and coworkers in 1995.[22] After more than 20 years, this material remains relatively under-explored. Previous studies

were mostly focused on its CO_2RR activity in ionic liquids or aprotic electrolytes with CO as the major reduction product.[23-25] Its potential in aqueous solution just starts to be unveiled and appreciated in recent years.[26-28] In order to promote and push its performance to the limit, designing and engineering Bi-based materials at the nanoscale becomes necessary. This is because enlarged surface areas and abundant structural defects associated with nanostructures generally afford them with heightened activities.[10, 11] Nevertheless, direct synthesis and control of metallic Bi nanostructures is experimentally challenging since Bi is a low melting point metal and susceptible to oxidation upon exposure to air. Herein, we report the facile solvothermal synthesis of ultrathin $Bi_2O_2CO_3$ nanosheets and their cathodic conversion to mesoporous Bi nanosheets. Final material exhibits impressive CO_2RR activity for selective CO_2 reduction to formate with a large cathodic current density and great Faradaic efficiency over a broad potential window. We further couple our CO_2RR electrocatalyst with an oxygen evolution reaction electrocatalyst in a full cell, and achieve solar-driven splitting of CO_2/H_2O to formate/O_2 at impressive energy conversion efficiency.

We started with the preparation of ultrathin two-dimensional (2D) $Bi_2O_2CO_3$ (BOC) nanosheets via a facile solvothermal reaction between $Bi(NO_3)\cdot 5H_2O$ and urea in N-methylpyrrolidine (NMP) (see the Experimental Section in Supporting Information). During the reaction, urea was gradually decomposed to NH_3 and CO_2, which then reacted with the Bi precursor. NMP was chosen as the reaction medium for its high boiling point and low viscosity. Our previous investigation showed that its suitable surface energy could effectively stabilize many 2D nanostructures.[29, 30] As-prepared BOC nanosheets have a typical light yellow color. Their powder X-ray diffraction (XRD) pattern exhibites diffraction peaks assignable to tetragonal $Bi_2O_2CO_3$ phase (**Figure 1a**), which consists of alternating $[Bi_2O_2]^{2+}$ layers and $[CO_3]^{2-}$ layers stacked along the *c*-direction. It is worth noting here that the (00*l*) diffraction peaks of BOC are considerably broadened compared to other diffraction peaks in XRD. This is the first indication of their ultrathin thickness along the *c*-direction, and the

average thickness is estimated to be ~4.2 nm based on the (002) peak using the Scherrer equation. Under SEM examination, BOC nanosheets are revealed to have a roughly square shape, which reflects the intrinsic four-fold symmetry of this layered tetragonal crystal along the *c*-direction (Figure 1b). Their ultrathin thickness is also inferred from their quasi-transparency to the electron beam. The lateral size of BOC nanosheets varies from 200 nm to 800 nm. Figure 1c presents the transmission electron microscopy (TEM) image of a typical BOC nanosheet. It has a smooth surface, clean edges, and sharp corners. Some dark stripes are observed on this nanosheet due to its slight deformation when relaxed on the lacy carbon support. Corresponding selected area electron diffraction (SAED) pattern reveals a single set of diffraction spots with four-fold symmetry consistent with tetragonal BOC. Its zone axis is indexed to be along the [001] direction, corroborating that each BOC nanosheet is terminated with the (001) plane (Figure 1d). Moreover, atomic force microscopy (AFM) analysis of two random nanosheets shows that their thickness is 3.5 nm and 7 nm, corresponding to two and four atomic layers, respectively (Figure 1e,f). This translates to a high aspect ratio of >100. Owing to its layered crystal structure, BOC is expected to preferentially grow in 2D, and as a result, many of its products have nanosheet or nanoplate morphologies.[31-33] However, the formation of atomic-thick BOC nanosheets here is incredible and not available from previous literature as far as we are aware. It is presumably due to their surface stabilization by NMP molecules. When NMP is replaced with other solvents such as water, ethylene glycol or dimethyl sulfoxide, the ultrathin nanosheet morphology is compromised (Figure S1, Supporting Information).

For the second step, as-prepared BOC nanosheets were used as the sacrificial template and cathodically converted to mesoporous Bi nanosheets. **Figure 2a** depicts the typical cyclic voltammetry (CV) curve of BOC nanosheets in N_2-saturated 0.5 M $NaHCO_3$. It exhibits a pronounced cathodic wave peaked at -0.15 V (versus reversible hydrogen electrode or RHE, the same hereafter), and two sequential anodic waves between 0.2 ~ 0.8 V. They correspond

to the redox interconversion between trivalent Bi and metallic Bi (according to the Pourbaix diagram of Bi[34]). Based on the CV curve, we determine that cathodic polarization within the potential window of -0.6 ~ -0.3 V could effectively convert BOC to metallic Bi without significant hydrogen evolution reaction (HER). Converted product is immediately removed from the electrolyte and characterized by XRD as shown in Figure 2b. In addition to signals from the electrode support, all diffraction peaks can be assigned to rhombohedral Bi metal free of starting BOC or other impurity phase. Very interestingly, the cathodic conversion doesn't compromise the structural integrity, and resultant product preserves the overall nanosheet morphology under SEM (Figure 2c). It only becomes clear from TEM that the original single-crystalline nanosheets transform to mesoporous Bi (mpBi) nanosheets upon reduction (Figure 2d). Close examination unveils that they are comprised of interconnected Bi nanoparticles about 5-10 nm in size, and are polycrystalline from SAED analysis (Figure 2e). These individual nanoparticles generally have a well-defined shape with exposed (012), (111) and (101) surface facets (Figure 2f and Figure S2, Supporting Information). Mesopore formation during the conversion from BOC to Bi is expected since this process involves a considerable volume condensation. However, it is remarkable that the conversion doesn't result in structural pulverization, and mpBi nanosheets even retain their overall square shape as shown in Figure 2d. Mesoporous nanosheets have enlarged surface areas, and therefore can maximize their contact with the liquid electrolyte. We estimate the electrochemical active surface area (ECSA) of mpBi nanosheets from the CV cathodic peak, and conclude that 13.4% of total Bi sites are electrochemically accessible (Figure S3, Supporting Information). This value is in a good agreement with the surface-to-volume ratio expected for 5-10 nm nanoparticles.

To evaluate the CO_2RR performance of the converted product, mpBi supported on carbon fiber paper was employed as the working electrode, and tested in membrane-separated two-compartment cell (see the Experimental Section in Supporting Information). In CO_2-saturated

0.5 M $NaHCO_3$ electrolyte, its negative-going polarization curve starts to take off at ~ -0.55 V, and then quickly rises to ~18 mA/cm^2 at -1.1 V (**Figure 3a**). Both values are markedly improved over commercial Bi nanopowder (Bi NP), which is measured to have an onset potential of ~ -0.65 V and cathodic current density of ~7 mA/cm^2 at -1.1 V. In the absence of any CO_2 feed gas (N_2-saturated 0.5 M $NaHCO_3$), the electrocatalytic activity of mpBi is exclusively attributed to HER — with a more negative onset potential and smaller cathodic current density, attesting to its relatively poor HER activity. Furthermore, in order to analyze the CO_2RR reduction product, electrolysis was performed at a few selected potentials between -0.5 V ~ -1.1 V for 1 h. Resultant gaseous products were measured by a gas chromatograph (GC) connected on line to the electrochemical cell; liquid products were collected at the end of electrolysis and measured by both nuclear magnetic resonance (NMR) spectroscopy and ion chromatography (IC) (Figure S4, Supporting Information). We find that formate is the predominant reduction product, together with small amounts of H_2 and CO. Their potential-dependent Faradaic efficiency is plotted in Figure 3b. Formate is first reproducibly detected at -0.57 V (corresponding to an overpotential of 0.38 V) on mpBi. Its Faradaic efficiency increases to >80% at -0.7 V, peaks at ~99% at -0.9 V, and then starts to slowly decline presumably because CO_2RR becomes diffusion-limited under large overpotentials. The contribution of H_2 or CO is mostly negligible. Only at <-1 V does the H_2 Faradaic efficiency start to grow over 5%. By contrast, control experiment with commercial Bi NP shows that its formate Faradaic efficiency reaches >80% only between -0.8 V ~ -0.9 V. Compared to most other CO_2RR materials, our mpBi not only features higher formate selectivity, but more importantly is able to maintain such high selectivity over a broad and mild potential window (>80% between -0.7 V ~ -1.1 V) (Figure 3c).[19, 20, 35-37] In order to demonstrate that formate comes from the reduction of CO_2, we additionally carried out control experiments in N_2-saturated 0.5 M $NaHCO_3$, and detected no formate or CO (Figure S5, Supporting Information). Furthermore, we calculated and compared the formate partial current density of mpBi and

commercial Bi NP as shown in Figure 3d. The former attains >17 mA/cm^2 at -1.0 V whilst the later never exceeds 4 mA/cm^2, underlining that CO_2RR on our mpBi nanosheets is significantly more efficient and selective. Tafel analysis suggests both mpBi and commercial Bi NP have a Tafel slope of 80-85 mV/decade (insert of Figure 3d), which is in good agreement with values previously reported for CO_2RR to formate on Sn-based materials.[17-19] Next, we assessed the stability of mpBi by biasing it at -0.8 V (corresponding to η = 0.6 V) for 12 h. Its time-dependent cathodic current density was recorded in Figure 3e, showing no sign of activity loss over the entire course of bulk electrolysis. Product analysis suggests that the average formate Faradaic efficiency is ~94%. Postmortem SEM examination of mpBi reveals that 2D nanosheet morphology survives from the long-term stability test (Figure S6, Supporting Information).

From above electrochemical measurements, it is established that our mpBi has the combination of high CO_2RR activity, great formate selectivity and satisfactory stability. It is superior to most previous Bi-based materials as well as other formate-producing CO_2RR electrocatalysts (such as Sn, In and N-doped carbon).[26, 27, 35-37] We attribute its great performance to the advantageous nanostructure. Density functional theory (DFT) calculations were performed to simulate the CO_2RR process on Bi (012), (111) and (101) planes (Figure 3f and Figure S7, Supporting Information). We find all the three surface planes favor the formation of OCHO* (ΔG = +0.19-0.41 eV, the intermediate to formate) over the formation of COOH* (ΔG = +0.82-0.86 eV, intermediate to CO) or H* (ΔG = +0.51-0.64 eV, intermediate to H_2). In particular, (101) and (111) planes can significantly stabilize OCHO* and therefore are the most active for formate production. This generally supports the observed high activity and Faradaic efficiency for formate in our experiments. Moreover, the CO_2RR performance is promoted by the unique 2D mesoporous nanosheet morphology with enlarged surface areas, abundant under-coordinated Bi sites and structural robustness.

As a step further, we pursued solar-driven CO_2/H_2O splitting to realize formate production using light as the only energy input (**Figure 4a**). 20 wt% Ir supported on Vulcan carbon black (Ir/C) was chosen as the electrocatalyst for oxygen evolution reaction (OER) by virtue of its excellent activity in neutral solution (albeit high cost and insufficient stability), and coupled with our mpBi to form a full catalytic cell. A commercial 1 cm^2 GaInP/GaInAs/Ge multi-junction solar cell was used for light harvesting from a 100 mW/cm^2 (1 sun) solar simulator. Under the light illumination, the solar cell has an open circuit voltage (V_{oc}) of 2.58 V and a short circuit current (J_{sc}) of 9.6 mA (Figure 4b). Its photovoltage is sufficient to turn on the CO_2RR/OER electrolysis. When the solar cell is used to power the catalytic cell, the working voltage and current can be derived from the intersection point between the *I-V* curve of the solar cell and the polarization curve of the catalytic cell, which are determined to be 2.5 V and 3.3 mA, respectively (Figure 4b). They nicely predict experimental results. During a 3 h solar-driven CO_2RR/OER electrolysis, the actual working voltage stays at 2.5 V (Figure 4c), and the actual current slightly decreases from ~3 mA to 1.9 mA due to the gradual deactivation of Ir/C (Figure 4d). The amount of formate produced in this period is analyzed to be 0.06 mmol. The overall solar-to-formate conversion efficiency is estimated to be 1.5%. Even though our efficiency is already higher than the typical efficiency of natural photosynthesis, we soberly realize that it is far from the limit that our device can possibly achieve and lower than the state-of-the-art devices recently reported (with solar-to-fuel conversion efficiency >5%)[[38, 39]] because of the mismatch between the I-V characteristics of the solar cell and the catalytic cell. The intersection point in Figure 4b is far away from the maximum power point on the *I-V* curve of the solar cell. In the future, if solar cells with a larger V_{oc} value (e.g. V_{oc} ~ 3 V, either using a single multijunction solar cell or two solar cells connected in series) could be employed to power our catalytic cell, the intersection point could be effectively pushed up, and so could the energy conversion efficiency.

In summary, we reported the preparation of 2D mesoporous Bi nanosheets from the cathodic conversion of atomic-thick $Bi_2O_2CO_3$ nanosheets. The final product had large surface areas while surprisingly retained the overall 2D structural integrity. When assessed as the CO_2RR electrocatalyst in 0.5 $NaHCO_3$, mpBi nanosheets enabled the efficient and robust CO_2 reduction to formate with the combination of large cathodic current density (~18 mA/cm^2 at -1.1 V), excellent selectivity (Faradaic efficiency ~100% over a broad potential window) and satisfactory stability (no activity or selectivity loss for 12 h). Their performance was superior to popular Sn-based materials as well as most other formate-producing CO_2RR electrocatalysts. mpBi nanosheets were also paired with Ir/C to achieve CO_2RR/OER full-cell electrolysis powered by GaInP/GaInAs/Ge multi-junction solar cell under 1 sun illumination at impressive energy conversion efficiency. Our study here unveils the great potential of nanostructured Bi materials for electrocatalytic and solar conversion of CO_2 to formate.

Supporting Information

Supporting Information is available from the Wiley Online Library or from the author.

Acknowledgements

We acknowledge the support from the Ministry of Science and Technology of China (2017YFA0204800), the National Natural Science Foundation of China (51472173 and 51522208), the Natural Science Foundation of Jiangsu Province (SBK2015010320), the Priority Academic Program Development of Jiangsu Higher Education Institutions and Collaborative Innovation Center of Suzhou Nano Science and Technology. J. Lu gratefully acknowledges support from the U. S. Department of Energy (DOE), Office of Energy Efficiency and Renewable Energy, Vehicle Technologies Office. Argonne National Laboratory is operated for DOE Office of Science by UChicago Argonne, LLC, under contract number DE-AC02-06CH11357.

Received: ((will be filled in by the editorial staff))
Revised: ((will be filled in by the editorial staff))
Published online: ((will be filled in by the editorial staff))

Conflict of Interest

The authors declare no conflict of interest.

References

[1] E. Romero, V. I. Novoderezhkin, R. van Grondelle, *Nature* **2017**, *543*, 355.
[2] R. E. Blankenship, D. M. Tiede, J. Barber, G. W. Brudvig, G. Fleming, M. Ghirardi, M. R. Gunner, W. Junge, D. M. Kramer, A. Melis, T. A. Moore, C. C. Moser, D. G. Nocera, A. J. Nozik, D. R. Ort, W. W. Parson, R. C. Prince, R. T. Sayre, *Science* **2011**, *332*, 805.
[3] J. Barber, *Chem. Soc. Rev.* **2009**, *38*, 185.
[4] Y. Tachibana, L. Vayssieres, J. R. Durrant, *Nat. Photonics* **2012**, *6*, 511.
[5] N. S. Lewis, D. G. Nocera, *Proc. Natl. Acad. Sci.* **2006**, *103*, 15729.
[6] K. Jiang, S. Siahrostami, A. J. Akey, Y. Li, Z. Lu, J. Lattimer, Y. Hu, C. Stokes, M. Gangishetty, G. Chen, Y. Zhou, W. Hill, W.-B. Cai, D. Bell, K. Chan, J. K. Noerskov, Y. Cui, H. Wang, *Chem* **2017**, *3*, 950.
[7] Y. Wu, J. Jiang, Z. Weng, M. Wang, D. l. L. J. Broere, Y. Zhong, G. W. Brudvig, Z. Feng, H. Wang, *ACS Cent. Sci.* **2017**, *3*, 847.
[8] Z. Weng, J. Jiang, Y. Wu, Z. Wu, X. Guo, K. L. Materna, W. Liu, V. S. Batista, G. W. Brudvig, H. Wang, *J. Am. Chem. Soc.* **2016**, *138*, 8076.
[9] M. S. Xie, B. Y. Xia, Y. Li, Y. Yan, Y. Yang, Q. Sun, S. H. Chan, A. Fisher, X. Wang, *Energy Environ. Sci.* **2016**, *9*, 1687.
[10] J. Wu, Y. Huang, W. Ye, Y. Li, *Adv. Sci.* **2017**, *4*, 1700194.
[11] D. D. Zhu, J. L. Liu, S. Z. Qiao, *Adv. Mater.* **2016**, *28*, 3423.
[12] N. Han, Y. Wang, L. Ma, J. Wen, J. Li, H. Zheng, K. Nie, X. Wang, F. Zhao, Y. Li, J. Fan, J. Zhong, T. Wu, D. J. Miller, J. Lu, S.-T. Lee, Y. Li, *Chem* **2017**, *3*, 652.
[13] X. Zheng, P. De Luna, F. P. García de Arquer, B. Zhang, N. Becknell, M. B. Ross, Y. Li, M. N. Banis, Y. Li, M. Liu, O. Voznyy, C. T. Dinh, T. Zhuang, P. Stadler, Y. Cui, X. Du, P. Yang, E. H. Sargent, *Joule* **2017**, *1*, 794.
[14] A. S. Agarwal, Y. Zhai, D. Hill, N. Sridhar, *ChemSusChem* **2011**, *4*, 1301.
[15] F. Joo, *ChemSusChem* **2008**, *1*, 805.
[16] S. Enthaler, J. von Langermann, T. Schmidt, *Energy Environ. Sci.* **2010**, *3*, 1207.
[17] Y. Chen, M. W. Kanan, *J. Am. Chem. Soc.* **2012**, *134*, 1986.
[18] S. Zhang, P. Kang, T. J. Meyer, *J. Am. Chem. Soc.* **2014**, *136*, 1734.
[19] F. Lei, W. Liu, Y. Sun, J. Xu, K. Liu, L. Liang, T. Yao, B. Pan, S. Wei, Y. Xie, *Nat. Commun.* **2016**, *7*, 12697.
[20] B. Kumar, V. Atla, J. P. Brian, S. Kumari, T. Q. Nguyen, M. Sunkara, J. M. Spurgeon, *Angew. Chem., Int. Ed.* **2017**, *56*, 3645.
[21] Y. Hori, K. Kikuchi, S. Suzuki, *Chem. Lett.* **1985**, *14*, 1695.
[22] S. Komatsu, T. Yanagihara, Y. Hiraga, M. Tanaka, A. Kunugi, *Denki Kagaku* **1995**, *63*, 217.
[23] J. L. DiMeglio, J. Rosenthal, *J. Am. Chem. Soc.* **2013**, *135*, 8798.

[24] J. Medina-Ramos, R. C. Pupillo, T. P. Keane, J. L. DiMeglio, J. Rosenthal, *J. Am. Chem. Soc.* **2015**, *137*, 5021.
[25] Z. Zhang, M. Chi, G. M. Veith, P. Zhang, D. A. Lutterman, J. Rosenthal, S. H. Overbury, S. Dai, H. Zhu, *ACS Catal.* **2016**, *6*, 6255.
[26] S. Kim, W. J. Dong, S. Gim, W. Sohn, J. Y. Park, C. J. Yoo, H. W. Jang, J.-L. Lee, *Nano Energy* **2017**, *39*, 44.
[27] J. H. Koh, D. H. Won, T. Eom, N.-K. Kim, K. D. Jung, H. Kim, Y. J. Hwang, B. K. Min, *ACS Catal.* **2017**, *7*, 5071.
[28] N. Han, H. Yang, J. Deng, J. Wu, Y. Li, Y. Wang, Y. Li, *Nat. Commun.* **2018**, *9*, 1320.
[29] J. Zhou, L. Wang, M. Yang, J. Wu, F. Chen, W. Huang, N. Han, H. Ye, F. Zhao, Y. Li, Y. Li, *Adv. Mater.* **2017**, *29*, 1702061.
[30] Y. Wang, J. Zhou, J. Wu, F. Chen, P. Li, N. Han, W. Huang, Y. Liu, H. Ye, F. Zhao, Y. Li, *J. Mater. Chem. A* **2017**, *5*, 25618.
[31] A. Umar, R. Ahmad, R. Kumar, A. A. Ibrahim, S. Baskoutas, *J. Alloys Compd.* **2016**, *683*, 433.
[32] Y. Liu, Z. Wang, B. Huang, K. Yang, X. Zhang, X. Qin, Y. Dai, *Appl. Surf. Sci.* **2010**, *257*, 172.
[33] P. Madhusudan, J. Ran, J. Zhang, J. Yu, G. Liu, *Appl. Catal., B* **2011**, *110*, 286.
[34] H. Y. Chen, L. Wu, C. Ren, Q. Z. Luo, Z. H. Xie, X. Jiang, S. P. Zhu, Y. K. Xia, Y. R. Luo, *J. Power Sources* **2001**, *95*, 108.
[35] Z. M. Detweiler, J. L. White, S. L. Bernasek, A. B. Bocarsly, *Langmuir* **2014**, *30*, 7593.
[36] H. Wang, J. Jia, P. Song, Q. Wang, D. Li, S. Min, C. Qian, L. Wang, Y. F. Li, C. Ma, T. Wu, J. Yuan, M. Antonietti, G. A. Ozin, *Angew. Chem., Int. Ed.* **2017**, *56*, 7847.
[37] S. Zhang, P. Kang, S. Ubnoske, M. K. Brennaman, N. Song, R. L. House, J. T. Glass, T. J. Meyer, *J. Am. Chem. Soc.* **2014**, *136*, 7845.
[38] Gurudayal, J. Bullock, D. F. Sranko, C. M. Towle, Y. Lum, M. Hettick, M. C. Scott, A. Javey, J. Ager, *Energy Environ. Sci.* **2017**, *10*, 2222.
[39] M. Schreier, F. Héroguel, L. Steier, S. Ahmad, J. S. Luterbacher, M. T. Mayer, J. Luo, M. Grätzel, *Nat. Energy* **2017**, *2*, 17087.

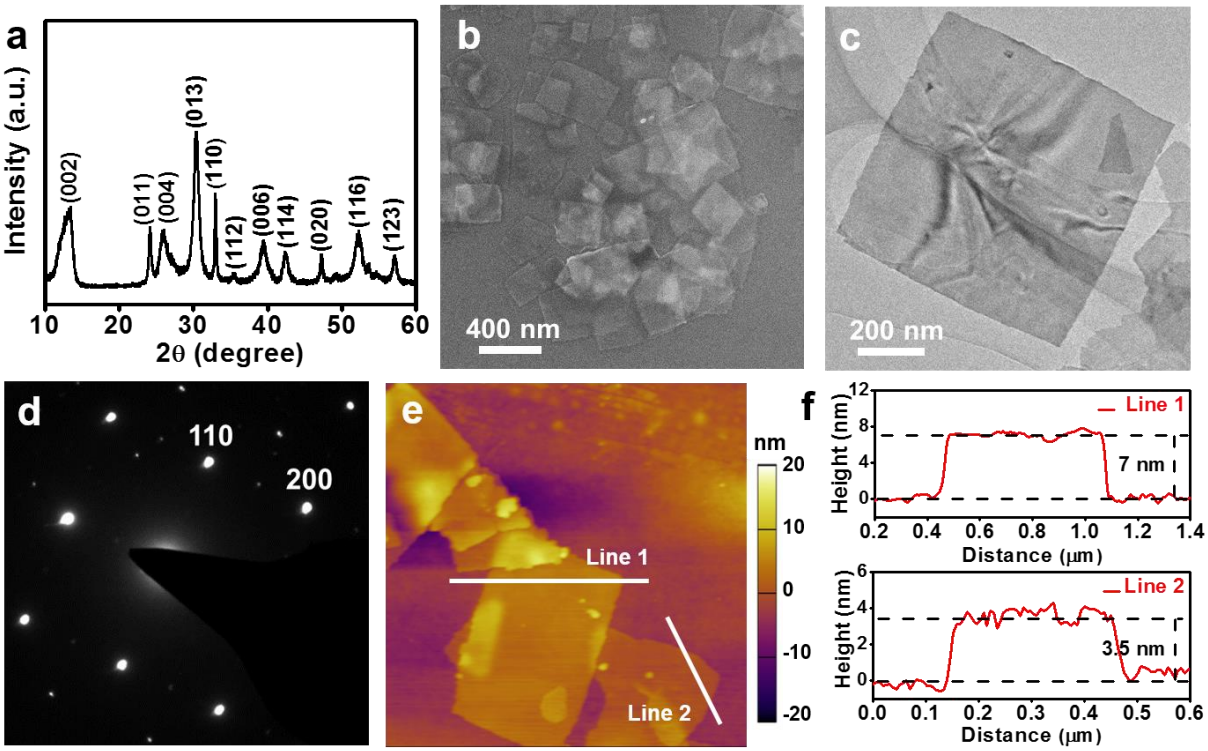

Figure 1. Structural characterizations of ultrathin BOC nanosheets. (a) XRD pattern, (b) SEM image, (c,d) TEM image and corresponding SAED pattern, and (e,f) AFM image and corresponding height profiles of BOC nanosheets derived from the first-step solvothermal synthesis.

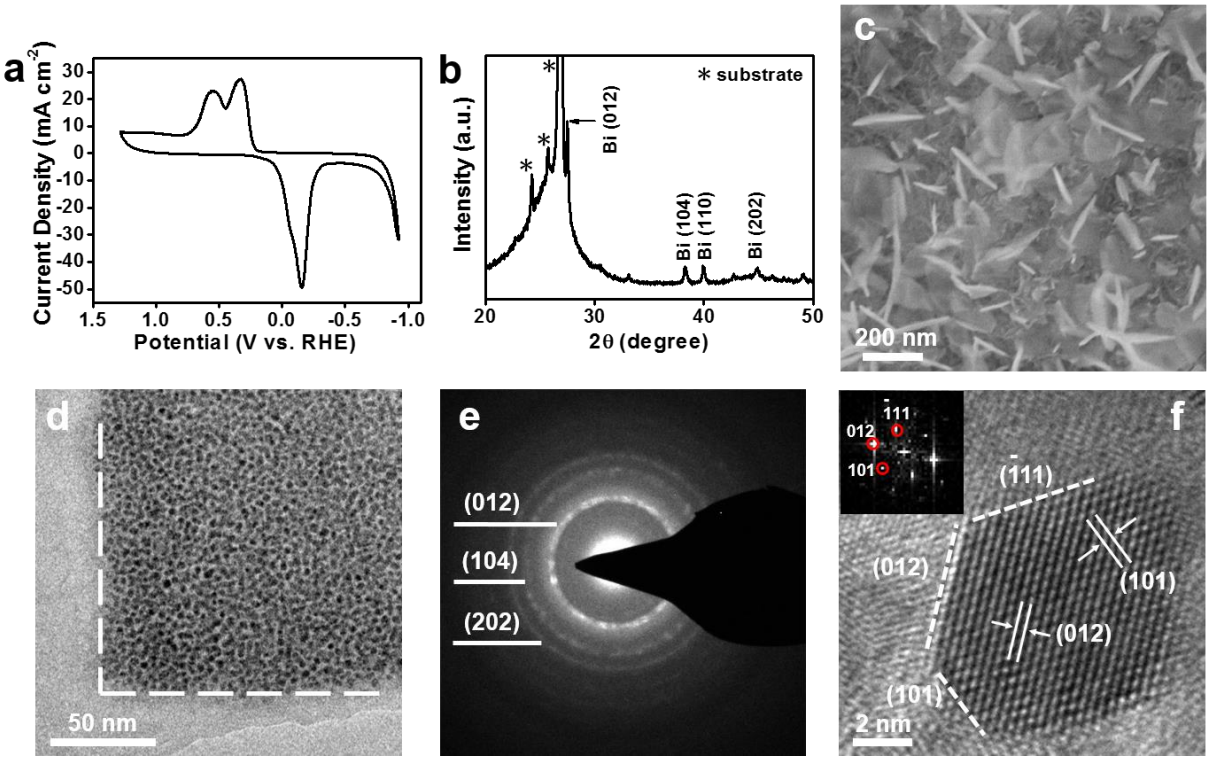

Figure 2. Structural characterizations of reduced mpBi nanosheets. (a) Typical CV curve of BOC showing its reduction to metallic Bi at cathodic potentials; (b) XRD pattern, (c) SEM image, (d,f) TEM images at different magnifications and (e) corresponding SAED pattern of reduced mpBi nanosheets**.**

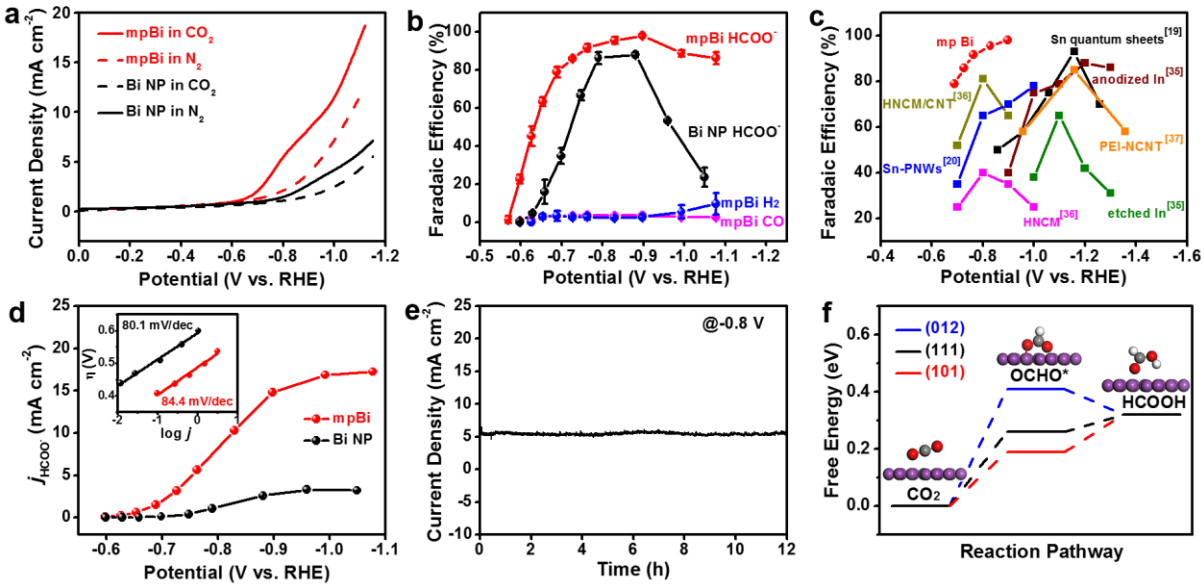

Figure 3. Electrocatalytic performance of reduced mpBi nanosheets for CO_2 reduction to formate. (a) Polarization curves of mpBi nanosheets and commercial Bi nanopowder in N_2- or CO_2-saturated 0.5 M $NaHCO_3$; (b) Faradaic efficiency of $HCOO^-$, H_2 and CO on mpBi nanosheets in comparison with Faradaic efficiency of $HCOO^-$ on commercial Bi nanopowder; (c) comparison of Faradaic efficiency of $HCOO^-$ in mpBi, Sn, In, and N-doped carbon; (d) formate partial current density of mpBi nanosheets and commercial Bi nanopowder, insert shows their corresponding Tafel slopes; (e) long-term stability of mpBi nanosheets at -0.8 V for 12 h; (f) free-energy diagram for HCOOH on Bi (101), (111), and (012) planes.

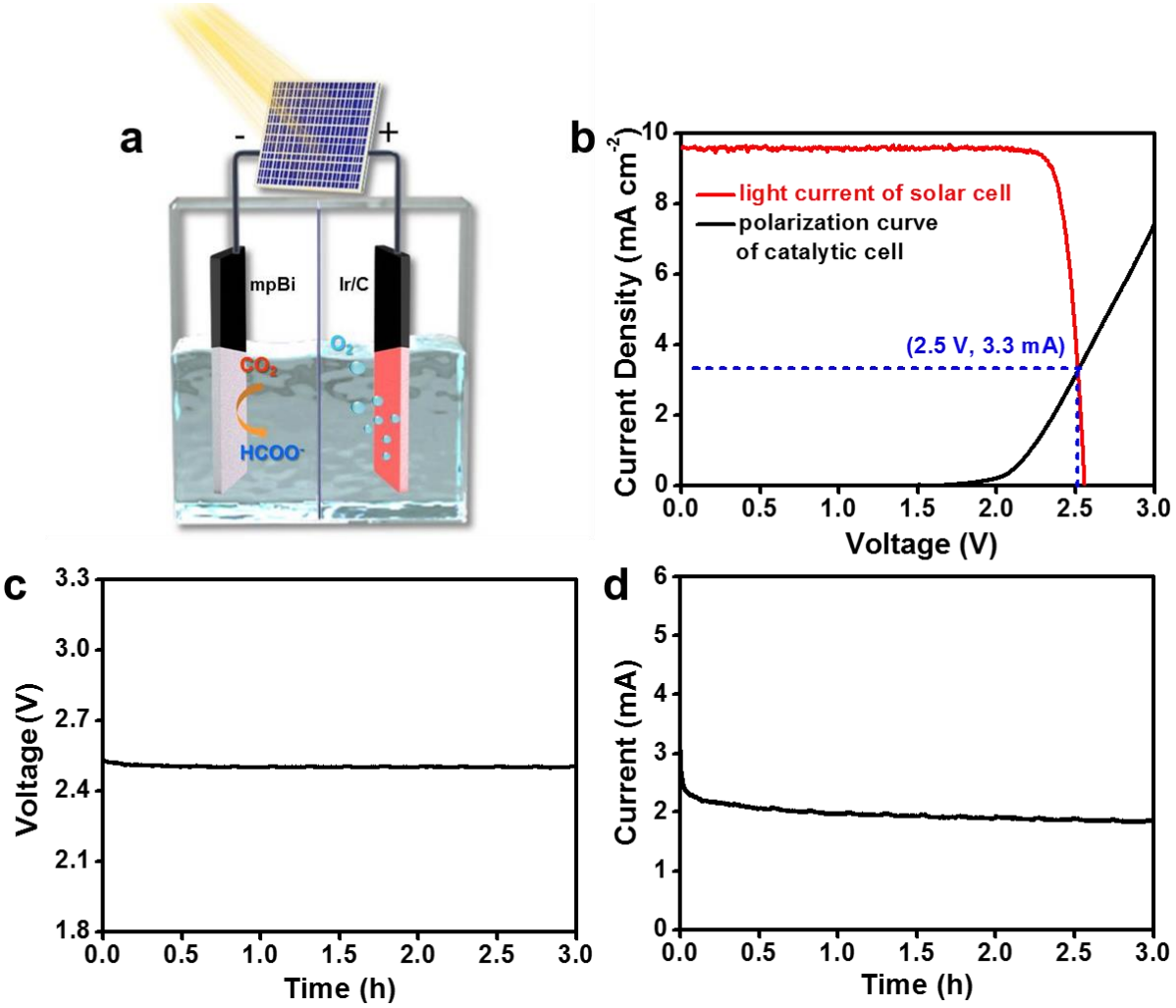

Figure 4. Solar-driven CO_2RR/OER full-cell electrolysis. (a) Schematic showing the experimental setup for the solar-driven full-cell electrolysis; (b) *I-V* curve of the GaInP/GaInAs/Ge multi-junction solar cell under illumination together with polarization curve of the catalytic cell, the intersection point predicts the experimental working voltage and current when the solar cell is used to power the catalytic cell; (c) voltage change and (d) current evolution during a 3 h solar-driven CO_2RR/OER electrolysis.

TOC figure

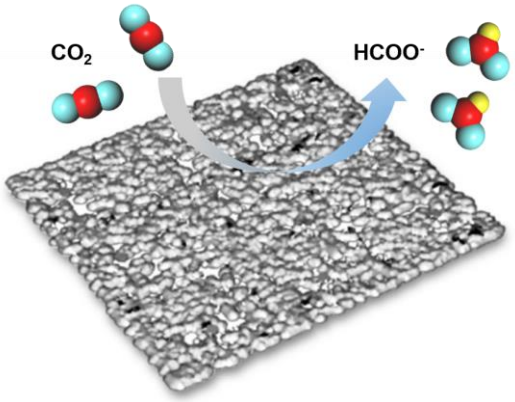

Cathodic transformation of atomic-thick $Bi_2O_2CO_3$ nanosheets to 2D mesoporous Bi nanosheets enabled the efficient CO_2 reduction to formate with large current density, excellent selectivity over a broad potential window and satisfactory stability.